Kusebauch, C., Oelze, M., Gleeson, S. A. (2018): Partitioning of arsenic between hydrothermal fluid and pyrite during experimental siderite replacement. - *Chemical Geology*, *500*, pp. 136—147.

DOI: http://doi.org/10.1016/j.chemgeo.2018.09.027

Chemical Geology 500 (2018) 136–147

Contents lists available at ScienceDirect

Chemical Geology

journal homepage: www.elsevier.com/locate/chemgeo

Partitioning of arsenic between hydrothermal fluid and pyrite during experimental siderite replacement

Christof Kusebauch[a,*], Marcus Oelze[a], Sarah A. Gleeson[a,b]

[a] Deutsches GeoForschungsZentrum GFZ, Telegrafenberg, 14473 Potsdam, Germany
[b] Freie Universität Berlin, Institute for Geosciences, Malteserstr. 74-100, 12249 Berlin, Germany

ARTICLE INFO

Editor: E. B Michael

Keywords:
Siderite
Replacement
Pyrite
Hydrothermal fluid
Arsenic partitioning
Carlin-type gold deposits

ABSTRACT

Arsenian pyrite is the major host mineral of gold in Carlin type gold deposit (CTGD) and forms during the interaction of H_2S bearing hydrothermal fluids with Fe-bearing carbonates (e.g., siderite, ankerite, Fe-rich dolomite) in the wall rock. Experimental replacement of siderite at hydrothermal conditions (i.e., 200 °C, Psat) was used to study the parameters that control the formation of CTGD pyrite (i.e., pH, time, aH_2S) and the partitioning of As between the hydrothermal fluid and newly formed pyrite.

Hydrothermal pyrite formed via replacement of siderite in experiments mainly occurs as two types: 1) porous, massive pyrite at alkaline pH conditions or 2) clusters of dense euhedral to anhedral pyrite grains at slightly acidic conditions (pH < 6). Longer experimental run times (2 weeks) lead to formation of type 2 pyrite at alkaline conditions and an increase in euhedral grain sizes in all conditions.

Concentration of As in newly formed pyrite depends strongly on the As concentration of the hydrothermal fluid used in the experiment. Calculated partition coefficients vary between 300 and 1700 with lowest D values at high As concentrations of the fluid. In the studied system As^{-1} substitutes for S^{-2} as indicated by the correlation of high As with low S concentrations. Experimental findings agree well with previous studies in natural CTGD on As substitution and the partitioning of As between ore stage pyrite and hydrothermal fluids trapped as fluid inclusions.

The newly constrained partition coefficients for As help to explain the large heterogeneity in natural CTGD pyrite compositions which is caused by changes in the fluid composition due to the strong partitioning of As into the forming pyrite.

1. Introduction

Iron-bearing sulfides (i.e. pyrite, pyrrhotite, chalcopyrite, arsenopyrite) are the host phases for elements of economic interest in many ore deposits. In particular, Carlin-type gold deposits (CTGD) are characterized by high concentrations (up thousands of ppm) of gold in pyrite that occurs either structurally bound together with arsenic or as nano-inclusions (Deditius et al., 2014; Palenik et al., 2004; Reich et al., 2005; Simon et al., 1999a). Deposits of the Carlin-type are typically hosted in calcareous sedimentary rocks (Cline et al., 2005; Saunders et al., 2014) and auriferous pyrite occurs either disseminated, as porous clusters or as epitaxial overgrowth on preexisting pyrite (Cline et al., 2005; Saunders et al., 2014 and references therein). Although the origin of the hydrothermal ore fluid is still under debate (see Cline et al., 2005; Emsbo et al., 2003; Large et al., 2011; Large et al., 2009; Large et al., 2016; Muntean et al., 2011), the fluid composition is well understood and fluid inclusions indicate homogenization temperatures between 180 and 240 °C, salinities of 3–6 wt% NaCl, CO_2 contents of 1–4 mol% and H_2S concentrations generally between 10^{-2} and $10^{-1}\,m$ (Cline et al., 2005; Large et al., 2016; Saunders et al., 2014; Su et al., 2009; and references therein).

Interaction of this H_2S rich hydrothermal fluid with reactive iron that originates either from the wall rock (Cail and Cline, 2001; Hofstra et al., 1991; Stenger et al., 1998) or is introduced via an additional fluid (Kesler et al., 2003; Ye et al., 2002) leads to the formation of pyrite rich in Au and As. Reactive iron in the carbonaceous wall rocks is contained in Fe-oxides, Fe-hydroxides, clays and in particular Fe-rich carbonates i.e., ankerite, siderite, and Fe-rich dolomite (Hofstra et al., 1991; Stenger et al., 1998). Decarbonation, or, sulfidation of the wall rock (i.e., desulfidation of fluid) is considered to be one of the major ore forming processes in CTGD and functions via fluid mediated replacement. Although the processes governing CTGDs have been studied in

* Corresponding author.
E-mail address: c.kusebauch@gfz-potsdam.de (C. Kusebauch).

https://doi.org/10.1016/j.chemgeo.2018.09.027
Received 20 March 2018; Received in revised form 18 September 2018; Accepted 20 September 2018
Available online 22 September 2018

detail in natural systems, experimental work on sulfidation reactions is very limited.

Experimental sulfidation of Fe-oxide and Fe-monosulfide to form Fe-disulfides (i.e., pyrite, marcasite) (Qian et al., 2010; Qian et al., 2011) showed that coupled dissolution-reprecipitation (Putnis, 2002) is the major process during sulfidation of Banded-Iron-Formations (Sung et al., 2009). Pyrite originating directly from solution forms via the transformation of early metastable monosulfide precursor phases (e.g., amorphous FeS, mackinawite, pyrrhotite, greigite) on different pathways (i.e., polysulfide, H_2S uptake, Fe-loss) (Benning et al., 2000; Schoonen and Barnes, 1991a; Schoonen and Barnes, 1991b; Schoonen and Barnes, 1991c). In contrast, pyrite formed from replacement can nucleate directly on the surface of the replaced mineral without the need of a metastable precursor phase (Qian et al., 2010).

The ore-stage pyrite in CTGD has characteristically high As concentrations (up to 19 wt%), which control the occurrence of Au in the pyrite ore (Deditius et al., 2014; Fleet and Mumin, 1997; Reich et al., 2005). Arsenic in pyrite can occur in different oxidation states which correspond to different crystallographic sites in the lattice and different substitution mechanisms: As^{-1} substitutes for S under reducing conditions and is most commonly found in CTGDs (Fleet and Mumin, 1997; Reich et al., 2005; Simon et al., 1999a) whereas cationic As (As^{+2}, As^{+3}, As^{+5}) substitutes for Fe under oxidizing conditions (Deditius et al., 2008; Qian et al., 2013). Incorporation of As into hydrothermal pyrite is generally described as a surface, and kinetically controlled, process (Deditius et al., 2008; Fleet and Mumin, 1997; Palenik et al., 2004). Although As in natural pyrite is intensively studied, and often used as a tracer for hydrothermal processes in natural rocks, studies investigating the partitioning of As between hydrothermal fluids and pyrite are rare (Deditius et al., 2014).

In this study, we investigated the interaction of siderite ($FeCO_3$) with a H_2S-containing hydrothermal fluid at 200 °C to mimic conditions of Carlin-type deposits showing wall rock sulfidation. On the one hand, the study investigated if the replacement of siderite is a critical process during formation of pyrite of Carlin-type deposits. On the other hand, the replacement of siderite was used to study the partitioning of As between the hydrothermal fluid and newly formed pyrite to better understand the interplay between As incorporation into pyrite and sulfidation of wall rock during formation of Carlin-type deposits.

2. Experimental and analytic methods

2.1. Experimental methods

Hydrothermal experiments were performed using in house manufactured PTFE-beakers (~6 ml) that were closed by conical shaped lids and placed in steel autoclaves. Autoclaves were placed in muffle furnaces at 200 °C for varying run durations of 22 to 450 h (Table 1). Weighed amounts of starting material (i.e., siderite or black shale containing siderite, 3–4 pyrite seeds, thioacetamide) were loaded together with ~4 ml of experimental fluid into the pre-cleaned PTFE beakers. Thioacetamide (CH_3CSNH_2) was used as the sulfidation agent as it breaks down upon heating to form H_2S. Although most experiments were done with a H_2S concentration of 0.05 *m* which is characteristic for Carlin type deposits (> 0.01; Simon et al., 1999b; Saunders et al., 2014; Hofstra and Cline, 2000), one experimental set (Sd2Py3-11) was done with H_2S concentrations varying from 0.005–0.5 *m* to investigate the influence of H_2S concentration on replacement. Hand-picked grains (n = 20–40, 125–250 μm, varying amounts) of natural siderite ($Fe_{0.6–0.9}(Mn,Mg)_{0.1–0.4}CO_3$) from two different localities (py1: Bad Schlema, Germany; py0: Schönbrunn, Germany) were used as starting material for each experiment. To promote epitaxial overgrowth, 3–4 grains of natural pyrite (< 0.1 mg, 125–250 μm) were added. Additionally to siderite experiments, two sets of experiments (Sd2Py12-14 and Sd2Py42-44) were conducted using mm-sized ships of natural black shales containing Fe-carbonate from the Selwyn Basin, Yukon, Canada (Magnall et al., 2016) to study siderite replacement in rocks that are similar to the host rocks of CTGD. Siderite replacement experiments were done at fluid buffered conditions and had high water-to-mineral ratios (by weight) of 200–2000 (Table 1). To control and fix the pH during experimental runs, most experiments were buffered in pH by using buffer solutions ($NH_4H_2PO_4$/$(NH_4)_2HPO_4$; CH_3COOH/CH_3COONa, H_3BO_3/NaOH) following Qian et al. (2010).

In partitioning experiments, As from an ICPMS standard solution (1000 ppm in 2% HNO_3; Sigma Aldrich) was added in concentrations ranging from 1 ppm to 100 ppm (see Table 1). Arsenic of the standard solution was introduced via dissolution of As_2O_3 and, therefore, cationic As (i.e., As^{+3}) was the dominant species. Additionally to As, we also added trace amounts of Au in a HCl based standard solution (0.05–10 ppm) to experimental runs. Partitioning of Au is not the focus of this paper and is, therefore, not discussed here. Here, all data for the As containing experiments are presented and experiments with the same As concentrations but varying Au concentration in the fluid can be seen as duplicates. Experimental run products (e.g., phase assemblage, pyrite appearance, progress of replacement) and partitioning of As are found to be independent of Au concentration in the experiment. In some experiments, beakers were flushed with Ar before closing to reduce fO_2 of the experiment which is induced by an airgap (Table 1). Oxygen fugacity of the experiments is controlled only by intrinsic phase stabilities and no phases were added to buffer fO_2.

Experiments were ended by taking the steel autoclaves out of the furnace and letting them cool slowly in air for about 1 h before the beakers were removed from the autoclaves. Due to the relatively slow cooling it cannot be ruled out that additional nm sized mineral phases precipitated and altered the fluid composition after cooling the experiment. Immediately after ending the experiment, beakers were weighed to check for leakage, opened and pH was measured at 25 °C. After separating fluid and solid run products, the fluids in the partition experiments were acidified using 50 μl concentrated suprapure HNO_3 and solids washed 3 times with deionized water and dried at 50 °C.

In many run solutions, a yellowish gel separated after acidifying, likely due to the reaction of the pH buffer with HNO_3. It was not possible to redissolve this gel which hindered the measurements of elements therein. Nevertheless, a clear filtrate without the gel component was measured for As, Au, Fe and Mn with ICP-MS using a ThermoFisher ELEMENT 2XR located at the GFZ Potsdam. Results can be found in the Supplementary table, but are not discussed further due to the problems encountered during acidification.

2.2. Analytical methods

2.2.1. Electron microprobe analysis (EMPA)

Several grains of solid run products as well as 1–2 pyrite seeds were carefully picked and mounted in epoxy and analyzed for major and trace element composition. Major and trace elements (i.e., S (Kα), Fe (Kα), As (Lα)) were analyzed using a JEOL JXA-8230 superprobe located at the GFZ Potsdam. Analytical conditions for quantitative analyses were: 15 kV, 40 nA, spot size (1–5 μm) depending on zonation and porosity, and long measurement times of 100 s for As. Standardization was done using natural and synthetic minerals (Fe, S: natural pyrite; As: gallium arsenide). Detection limits for As in pyrite are around 70 ppm.

2.2.2. Mass spectroscopy (LA-ICP-MS)

Laser ablation ICP-MS was carried out using the Analyte Excite 193 nm ArF* excimer-based laser ablation (LA) system (Teledyne Photon Machines, Bozeman, MT, USA), coupled to the quadrupole-ICP-MS iCAP from Thermo Scientific. The LA-system is equipped with a HelEx II 2-volume ablation cell. Helium was used as a carrier gas for aerosol transport from the sample surface to the ICP and was mixed downstream with Ar as a make-up gas before entering the plasma. Operational parameters of the ICP-MS instrument and LA-unit were

Table 1
Experimental conditions and As concentrations.

Sample	T (°C)	t(h)	Sol. As (ppm)	Sol. Au (ppm)	pH	pH calc at 200 °C[a]	$pH_{25°C}$ meas. exp.[b]	Solid	W/r	Molal H_2S in fluid	Media above fluid	Assemblage	LA-ICPMS ppm As	±	s.d.	EMPA PyII ppm As	±	s.d.	D_{As}[f]
Sd2Py3	200	168	–	–	–	–	5.4	Sd0	307	0.024	Ar	Po, Mag, Sd							
Sd2Py4	200	168	–	–	–	–	5.1	Sd0	219	0.005	Ar	Po, Mag, Sd							
Sd2Py5	200	168	–	–	–	–	5.3	Sd0	335	0.051	Ar	Py, Po, Mag							
Sd2Py6	200	48	–	–	–	–	5.7	Sd0	361	0.013	Ar	Py, Po, Sd, ± Mag							
Sd2Py7	200	48	–	–	–	–	5.6	Sd0	341	0.007	Ar	Po, Mag, Sd							
Sd2Py8	200	48	–	–	–	–	6.0	Sd0	427	0.053	Ar	Py, Po, Sd							
Sd2Py9	200	21	–	–	–	–	6.1	Sd0	286	0.110	Ar	Py, Po, Sd							
Sd2Py10	200	21	–	–	–	–	6.3	Sd0	330	0.511	Ar	Py							
Sd2Py11	200	21	–	–	–	–	6.3	Sd0	313	0.244	Ar	Py							
Sd2Py12	200	168	–	–	–	–	8.3	BS	111	0.010	Ar	Py, Po							
Sd2Py13	200	168	–	–	–	–	6.1	BS	111	0.058	Ar	Py, Po							
Sd2Py14	200	168	–	–	–	–	7.0	BS	103	0.108	Ar	Py, Po							
Sd2Py15	200	22	–	–	pH4[c]	4.7	4.4	Sd1	1604	0.050	Ar	Py, ± Po							
Sd2Py16	200	22	–	–	pH 7[d]	6.8	6.7	Sd1	1464	0.053	Ar	Py, Sd							
Sd2Py17	200	22	–	–	pH 9[e]	8.3	8.1	Sd1	1617	0.053	Ar	Py, Sd							
Sd2Py18	200	46	–	–	pH4[c]	4.7	4.4	Sd1	1537	0.050	Ar	Py, ± Po							
Sd2Py19	200	46	–	–	pH 7[d]	6.8	6.6	Sd1	1365	0.051	Ar	Py, Sd							
Sd2Py20	200	46	–	–	pH 9[e]	8.3	8.2	Sd1	1682	0.051	Ar	Py, Sd							
Sd2Py21	200	166	–	–	pH4[c]	4.7	4.6	Sd1	1484	0.051	Ar	Py, ± Po							
Sd2Py22	200	166	–	–	pH 7[d]	6.8	6.9	Sd1	1718	0.051	Ar	Py, Sd							
Sd2Py23	200	166	–	–	pH 9[e]	8.3	8.7	Sd1	1547	0.051	Ar	Py, Sd, ± Po							
Sd2Py30	200	163	100	0.1	–	–	9.4	Sd1	1557	0.047	Ar	Py, ± Po	71,461	±	24,902	73,274	±	21,826	715
Sd2Py31	200	163	100	1	–	–	9.6	Sd1	1841	0.047	Ar	Py, ± Po	50,450	±	18,075	61,486	±	8070	505
Sd2Py32	200	163	100	10	–	–	9.1	Sd1	1300	0.048	Ar	Py, ± Po	42,466	±	5709	56,039	±	19,466	425
Sd2Py33	200	450	1	0.05	pH4[c]	4.7	4.3	Sd1	1758	0.056	Ar	Py, ± Po	1282	±	833	1395	±	1990	1282
Sd2Py34	200	450	1	0.5	pH4[c]	4.7	4.3	Sd1	2240	0.052	Ar	Py, ± Po	1545	±	463	715	±	882	1545
Sd2Py35	200	450	1	5	pH4[c]	4.7	4.2	Sd1	1610	0.053	Ar	Py, ± Po	224	±	141	1190	±	1093	1190[f]
Sd2Py36	200	450	5	0.05	pH4[c]	4.7	4.4	Sd1	2235	0.051	Ar	Py, ± Po	4420	±	2147	3808	±	3490	884
Sd2Py37	200	450	5	0.5	pH4[c]	4.7	4.4	Sd1	2116	0.053	Ar	Py, ± Po	3994	±	2375	1927	±	2062	799
Sd2Py38	200	450	5	5	pH4[c]	4.7	4.3	Sd1	1916	0.051	Ar	Py, ± Po	4515	±	2490	2236	±	2129	903
Sd2Py42	200	168	100	0.1	pH5[c]	5.8	8.9	BS	287	0.053	air	Py, ± Po	31,205	±	12,729				312
Sd2Py43	200	168	100	1	pH5[c]	5.8	9.2	BS	200	0.056	air	Py, ± Po	46,661	±	20,663				467
Sd2Py44	200	168	100	10	pH5[c]	5.8	8.2	BS	279	0.054	air	Py, ± Po	25,868	±	5859				259
Sd2Py45	200	168	50	0.05	pH5[c]	5.8	5.4	Sd1	2124	0.051	air	Py, ± Po	38,700	±	15,771	36,965	±	13,583	774
Sd2Py46	200	168	50	0.5	pH5[c]	5.8	5.4	Sd1	1683	0.049	air	Py, ± Po	32,086	±	6641	40,595	±	14,934	642
Sd2Py47	200	168	50	5	pH5[c]	5.8	5.3	Sd1	1609	0.050	air	Py, ± Po	34,485	±	4527	34,300	±	11,942	690
Sd2Py48	200	168	100	0.1	pH5[c]	5.8	8.1	Sd1	1561	0.053	air	Py, ± Po	30,065	±	2923	45,953	±	20,994	301
Sd2Py49	200	168	100	1	pH5[c]	5.8	8.8	Sd1	2028	0.049	air	Py, ± Po	68,688	±	14,609	54,527	±	10,124	687
Sd2Py50	200	168	100	10	pH5[c]	5.8	7.9	Sd1	1283	0.062	air	Py, ± Po	31,703	±	4106	37,465	±	16,109	317
Sd2Py51	200	332	10	0.05	pH5[c]	5.8	5.1	Sd1	1642	0.051	air	Py, ± Po	16,760	±	2532	21,290	±	15,748	1676
Sd2Py52	200	332	10	0.1	pH5[c]	5.8	5.2	Sd1	1633	0.051	air	Py, ± Po	12,336	±	4175	12,297	±	9038	1234
Sd2Py53	200	332	10	0.5	pH5[c]	5.8	5.2	Sd1	1515	0.053	air	Py, ± Po	15,966	±	6192	20,865	±	11,208	1597
Sd2Py54	200	332	20	0.05	pH5[c]	5.8	5.2	Sd1	1560	0.055	air	Py, ± Po	21,137	±	3729	24,365	±	16,171	1057
Sd2Py55	200	332	20	0.1	pH5[c]	5.8	5.2	Sd1	1552	0.054	air	Py, ± Po	26,183	±	9615	15,323	±	13,778	1309
Sd2Py56	200	332	20	0.5	pH5[c]	5.8	5.2	Sd1	1500	0.053	air	Py, ± Po	25,213	±	3304	29,500	±	12,315	1261

[a] pH @200 °C was calculated using PHREEQC.
[b] pH @25 °C was measured immediately after the experiment was ended and cooled to 25 °C.
[c] pH buffer CH2COOH/CH3OONa: 0.1656 M/0.0343 M (for pH 4); 0.06/0.14 (for pH 5).
[d] pH buffer NH4H2PO4/(NH4)2HPO4: 0.0685 M/0.1314 M.
[e] pH buffer H3BO3/NaOH: 0.05 M/0.021 M.
[f] D values calculated using EMPA data.

tuned for maximum sensitivity, low oxide formation based on the $^{232}Th^{16}O/^{232}Th$ ratio and low laser-induced elemental fractionation based on the $^{232}U/^{232}Th$ ratio using NIST SRM 610. For analysis we measured the following isotopes: ^{24}Mg, ^{34}S, ^{55}Mn, ^{57}Fe, ^{75}As and ^{197}Au. We used ^{57}Fe as internal standard and the certified reference material MASS1 for calibration for all elements. Samples were ablated with spot sizes between 20 and 40 μm, for 30 s with a repetition rate of 10 Hz and an energy density of 2–3 J/cm^2. The data was reduced using the commercial software Iolite (Paton et al., 2011) and the data reduction scheme X_trace_elemets_IS (Woodhead et al., 2007). Reproducibility of As concentrations is better than 7% based on multiple measurements of standard material (i.e., NIST610, MASS1).

The LA-ICP-MS spot size was usually bigger than individual grains of newly formed pyrite, and so the data represent an average of different grains and zones. Nevertheless, concentrations quantified by LA-ICP-MS are in agreement with concentrations measured by EMPA.

2.2.3. Microscopy and Raman

Additionally to compositional analysis of iron bearing phases, we used Raman spectroscopy (LABRAM HR Evolution, HORIBA located at the GFZ, Potsdam) on selected samples and petrographic microscopy to identify different types of newly formed pyrite. Obtained Raman spectra were compared to reference spectra of common sulfides provided by the RRUFF data base (see supplements for details). Spectra were taken using a 532 nm laser, 50× magnification and grating of 1800.

3. Results

3.1.1. Replacement and texture formation

The sulfidation reaction i.e. replacement of Fe-rich carbonates by Fe-sulfides can be illustrated by 2 distinct reactions: dissolution of carbonate to release Fe into fluid or fluid interlayer under neutral to acidic pH conditions of experiments:

$$FeCO_3\,(s) + 2H^+\,(aq) \leftrightarrow Fe^{2+}\,(aq) + CO_2\,(aq) + H_2O \quad (1)$$

and the formation of sulfide to precipitate Fe and S into a mineral phase (i.e. pyrite) under reducing conditions

$$Fe^{2+}\,(aq) + 2\,H_2S\,(aq) \leftrightarrow FeS_2\,(s) + 2H^+\,(aq) + H_2\,(aq) \quad (2)$$

resulting in the overall redox reaction

$$FeCO_3\,(s) + 2\,H_2S\,(aq) \leftrightarrow FeS_2\,(s) + H_2O + H_2\,(aq) + CO_2\,(aq) \quad (3)$$

Siderite replacement by pyrite can be described as a coupled dissolution-reprecipitation reaction (Putnis, 2002) and is considered to be pseudomorphic at $pH_{25°C} > 5$ as the external dimensions of the carbonate grains are preserved. Depending on experimental conditions (i.e., run time, pH, H_2S concentration, trace element concentrations) different newly formed Fe-bearing minerals (i.e., magnetite, pyrite, pyrrhotite, arsenopyrite) are observed (see Table 1) of which pyrite is the most abundant and most important phase. In general, two different pyrite types are formed; type 1) 'porous pyrite' appears massive under the transmitted light microscope but has a high density of nm sized pores under the electron microscope (Fig. 1a). Microprobe analyses give totals of 85–93% due to the highly porous nature of this material. This phase has a S/Fe ratio of ~2 identical to pyrite. Raman spectra of the porous phase show characteristic peaks similar to pyrite that are shifted towards lower wavenumbers, which probably results from the nano/microporous structure (see supplements Fig. S1). Type 2) 'dense pyrite' either appears as euhedral to sub-euhedral grains of a few μm size that tend to form clusters (Fig. 1a) or appears as elongated anhedral clusters within pyrite of type 1. Porous and dense pyrite also forms an intermediate phase, producing a mesh of nm to μm sized pyrite grains with open pore space between individual crystallites.

Two experiments (Sd2Py 45, 55) formed pyrite that is rounded and best described as framboidal (Fig. 1c). This pyrite type is found mainly on the outside of pseudomorphically replaced grains.

Apart from pyrite that formed via replacement of siderite, pyrite formed as overgrowth on the pyrite seeds or as replacement rims of these seeds was rarely observed and occur only in experiments with lowest pH (Fig. 1b).

3.1.2. H_2S concentration dependency

The influence of the H_2S concentration on the replacement was studied at fluid-mineral ratios of ~300. The H_2S activity is the major control on the stability of different Fe-bearing phases in the system. Low starting H_2S concentrations (0.005–0.01 *m*) lead to a preferred replacement of siderite by pyrrhotite and magnetite (Fig. 2a). At H_2S concentrations ranging from 0.01 to 0.05 *m*, a complex replacement texture involving pyrite, pyrrhotite and magnetite is formed. The former siderite grain has a mineralogical zonation inwards, with euhedral pyrite and pyrite clusters (Fig. 2b) on the rim, a zone of pyrrhotite needles, and then a zone of μm sized euhedral magnetite towards the core. In some experiments, siderite still exists as remnants in core regions. Euhedral magnetite is also found within existing siderite along the former cleavage planes system of the carbonate (Fig. 2a,b). With increasing H_2S (> 0.05) pyrite becomes the dominant phase and magnetite is no longer formed. Pyrrhotite can still be present and is often found in the cores of replaced grains. In some experiments, pyrite and pyrrhotite are intergrown or euhedral pyrite forms as an overgrowth on pyrrhotite (Fig. 2c).

3.1.3. Run time and pH dependency

Time and pH dependency of siderite replacement and the formation of pyrite were studied by varying experimental run durations from 22 to 450 h and $pH_{25°C}$ from ~4.4 to ~8.6. Conditions were always strongly fluid-dominated (f/m ratio ~1600) and H_2S concentration was kept constant at 0.05 *m*. The experimental system was always oversaturated in H_2S with respect to pyrite formation.

At short runs and high $pH_{25°C}$ (6.6–8.6) porous pyrite (type 1) dominates the run products, whereas in long runs and at alkaline conditions, euhedral pyrite (type 2) becomes more abundant and is also larger in size (Fig. 3). At low $pH_{25°C}$ conditions of ~4.4, only euhedral pyrite or clusters of euhedral pyrite exist and crystal size increases with duration (Fig. 3). Although all experimental conditions were chosen to stabilize only pyrite, small amounts of pyrrhotite (either intergrown with or as inclusions in euhedral pyrite) were observed independent of run duration.

3.2. Experiments using siderite-bearing black shale

The replacement behavior of siderite was not only studied in pure siderite-fluid systems but also in natural sedimentary rocks. We performed experiments using one or two, mm-sized chips of natural black shales containing siderite. These samples were chosen as an analogue of

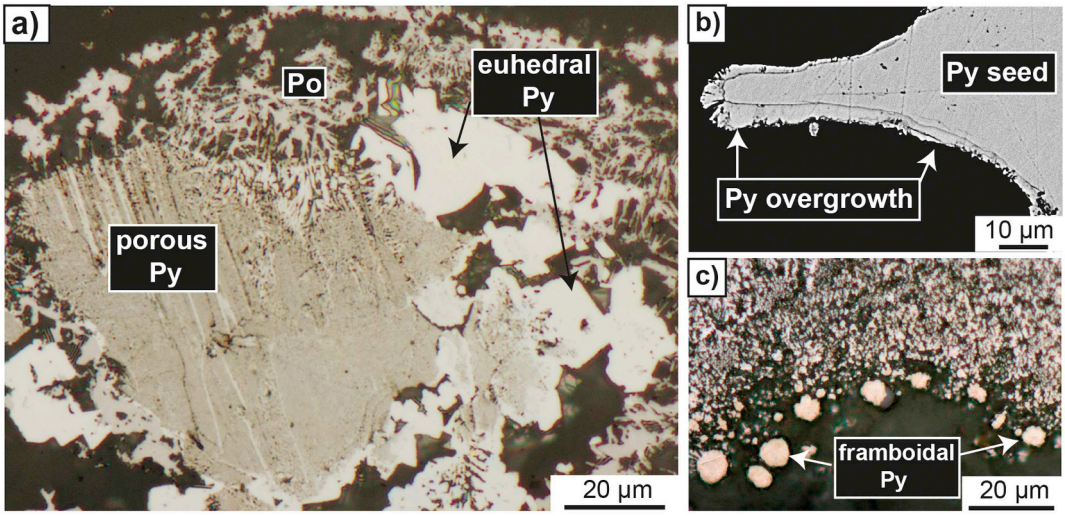

Fig. 1. Textures of different pyrite types: a) different types of pyrite resulting from replacement of siderite; b) newly formed pyrite overgrowing a pyrite seed at low pH (4.2); c) framboidal pyrite on the edge of replacement pyrite.

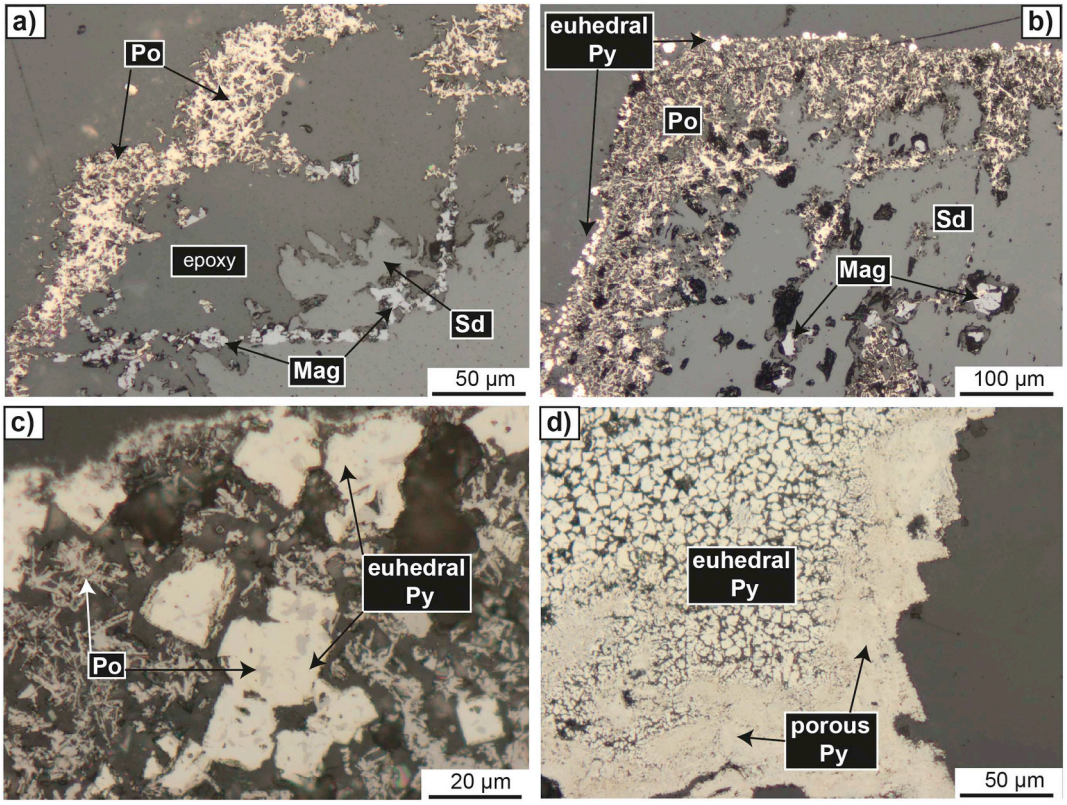

Fig. 2. Textures of siderite replacement with increasing H_2S concentration: a) 0.007 *m*; b) 0.013 *m*; c) 0.053 *m*; d) 0.51 *m*.

potential CTGD wall rocks that also contain reactive iron in the form of Fe-carbonates (i.e., ankerite and siderite). The grain size of siderite in this sediment is in the range of 50–200 µm and, therefore, similar to that used in siderite only experiments. Replacement textures from these experiments are very similar to those observed from experiments using pure siderite (Fig. 4). Siderite in black shale sediments is mainly replaced by porous pyrite. A small fraction of the porous pyrite recrystallizes into euhedral pyrite crystals. These observations are in agreement with observations from the siderite only experiments, where similar run durations and a relatively alkaline $pH_{25°C}$ of 8–9 led to the same results. Although part of the experiments were done using a pH buffered solution, the quench $pH_{25°C}$ was always higher than the desired $pH_{25°C}$ (see Table 1). The rise in pH is probably due to the usage of a complex multiphase natural rock rather than a single phase leading to a more rock controlled system.

3.3. Distribution of arsenic

Partitioning of As between hydrothermal fluids and newly formed pyrite was studied by adding trace concentrations (1–100 ppm) of As to experimental fluids. Partitioning experiments using pure siderite were exclusively performed at high fluid-to-mineral ratios > 1300, slightly acidic conditions and H_2S concentrations of 0.05 M (Table 1). Arsenic was measured in newly formed sulfides by EMPA and LA-ICP-MS. Each of the two methods has their strength and weaknesses with respect to the purpose of this study and gave complementary results. EMPA measurements facilitated a high spatial resolution (i.e., spotsize < 1–5 µm) and was used to characterize As concentrations of co-existing pyrite types (e.g., framboidal, porous, euhedral) as well as pyrrhotite at high concentration levels (> 70 ppm).

LA-ICP-MS was used to characterize larger areas (using a 20–40 µm spot size) of a representative replacement assemblage at concentration levels down to few ppm. The analyzed area of LA-ICP-MS measurements exceeds the size of individual crystals, hence As values are always an average of individual euhedral pyrite crystals or a mixture of euhedral, porous pyrite, and/or pyrrhotite. Special care was taken during LA-ICP-MS measurements to analyze areas with a high density of euhedral pyrite. Nevertheless, the large heterogeneity within the euhedral type of pyrite as observed by EMPA is able to explain also the variance in LA-ICP-MS measurements.

In general, averaged results for euhedral pyrite of each experiment quantified using both methods agree within individual standard deviation (Fig. 5). Furthermore, compositions of newly formed pyrite from duplicate experiments overlap well within their respective uncertainties. Only As concentrations of experiment Sd2Py35 quantified by LA-ICP-MS deviate from EMPA measurements and also from results of duplicate experiments. Pyrite grains of this particular experiment are smaller than usual and only three LA-ICP-MS spots could be set on the sample. Therefore, we consider the EMPA measurements of experiment Sd2Py35 more trustworthy and will use EMPA data rather than LA-ICP-MS in the discussion.

3.3.1. Arsenic in different sulfides and pyrite types

In individual samples containing more than one type of pyrite, porous pyrite, generally, has lower As values compared to euhedral pyrite (Fig. 6). This behavior can be explained by the non-equilibrium conditions of fast replacement reactions that form porous pyrite, in contrast to euhedral pyrite that grew more slowly under partially equilibrated conditions. Long run durations and low pH of the experiments lead to higher degree of recrystallization of the porous pyrite. Minor framboidal pyrite has a similar composition as euhedral pyrite in one experiment (Sd2Py55) but distinctively lower As values in the experiment (Sd2Py45). As framboidal pyrite in our experiments occurs only on the outside of former siderite grains and not as a direct result of replacement, framboidal pyrite may precipitate as a very late product during quenching of the experiment. In this case, it will form rather rapidly under disequilibrium conditions that might explain the inconsistent incorporation of trace elements. It may also form freely within

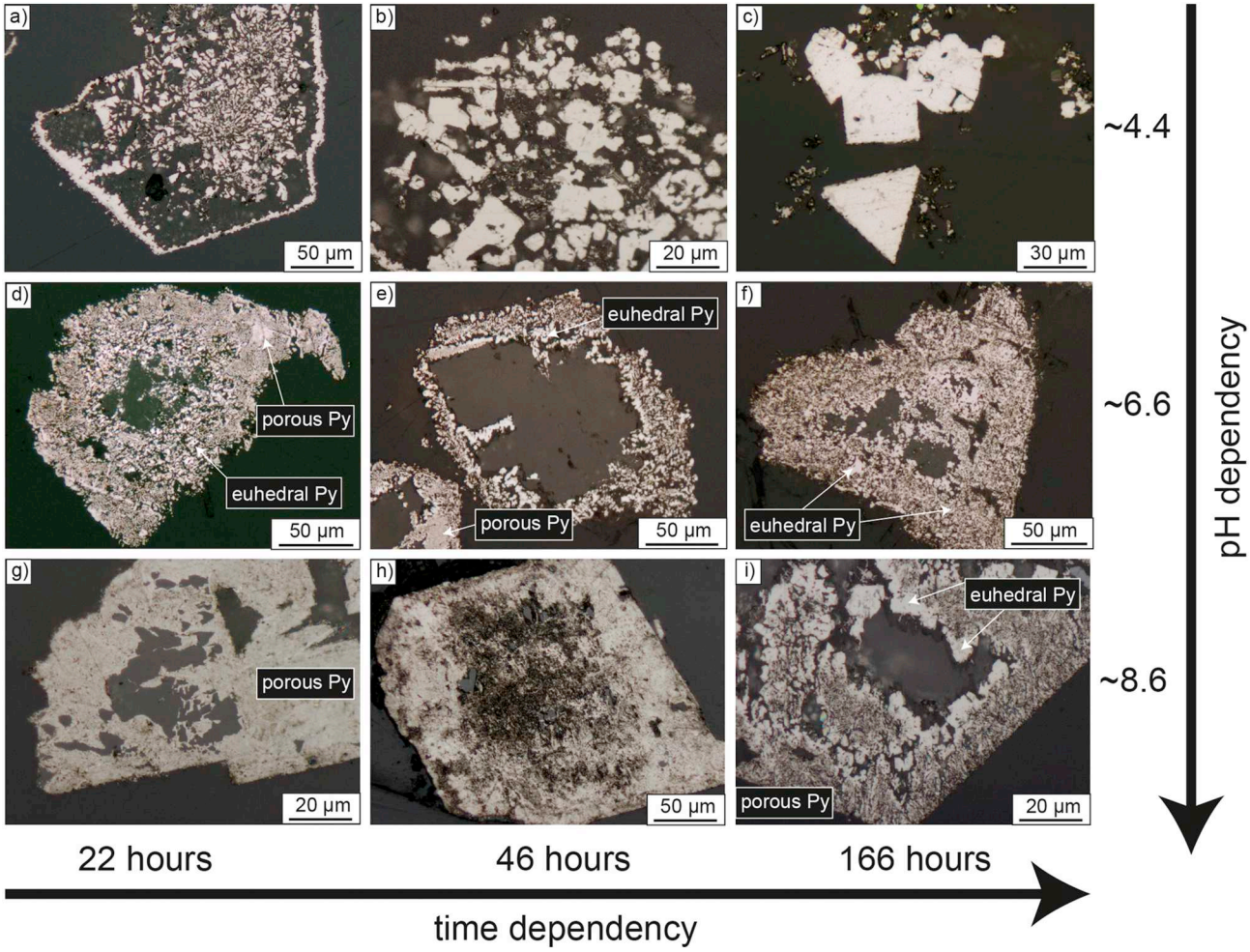

Fig. 3. Increasing size and abundance of euhedral pyrite with increasing run duration and decreasing pH.

the bulk fluid in the first place and is later attached to the replaced pyrite. However, framboidal pyrite is only a very minor pyrite type formed under experimental conditions.

Pyrrhotite, occurring either as dense single crystals or as aggregated needles, has consistently lower As concentrations compared to coexisting pyrite (Fig. 6). This behavior is also observed in natural pyrrhotite coeval with pyrite (Thomas et al., 2011) and is the result of a lower solubility of As in the pyrrhotite structure compared to pyrite. The low As values of pyrrhotite implies that LA-ICP-MS measurements of areas with larger amounts of pyrrhotite will lead to an underestimation of As in the actual pyrite. Consequently, LA-ICP-MS concentrations of euhedral pyrite should only be seen as minimum values.

3.3.2. *Arsenic partitioning between pyrite and hydrothermal fluid*

The As concentration of newly formed pyrite depends strongly on the starting composition of the experimental fluid (Fig. 7). Lowest values of 250–1500 ppm As were measured in pyrite from experiments using solutions containing 1 ppm, whereas highest values of 7–8 wt% As were measured in pyrite from experiments using solutions containing 100 ppm As (Fig. 7). Measurements of different pyrite grains from individual experiments by EMPA show a large variability in As (Table 1).

Nernst partition coefficients (D values) were calculated using the following expression:

$$D = c_{As}^{(py)} / c_{As}^{(fl)} \quad (4)$$

with c_{As} being the concentration by mass of As in pyrite and fluid, respectively. For the calculation of individual partition coefficients, we use the starting composition of experimental fluids and averaged As concentrations of euhedral pyrite measured with LA-ICPMS. Fluid-to-mineral ratios of siderite replacement experiments studying As partitioning were in the range of 1300–2200 and, therefore, experiments were strongly fluid buffered. Hence, the fluid composition is stable over the whole duration of the experiment. Calculated partition coefficients of all experiments range between 286 and 1676, showing that As is highly compatible in hydrothermally precipitated pyrite. In general, highest D values of around 1000 are homogenous over fluid compositions ranging from 1 to 20 ppm and agree within individual errors (Fig. 8). The observed decrease in D values down to ~300 at high As concentration 50–100 ppm As in fluid is caused by approaching the solubility limit of As in pyrite, which limits the As concentration to 7–8 wt% (see Section 4.2).

4. Discussion

4.1.1. *Sulfide stabilities during progressing siderite replacement*

Experimental observations (i.e., different sulfide phases, sequence of replacement rims) can be explained by two different effects: 1) compositional evolution of the system under equilibrium conditions or 2) metastable formation of pyrrhotite under disequilibrium conditions. In the first case, the different zones (i.e., pyrite, pyrrhotite, magnetite) result directly from thermodynamic stabilities of Fe-bearing phases at low oxygen fugacity and a decreasing H_2S fugacity (Fig. 9). Due to the relatively low fluid to mineral ratio, S will be consumed from the fluid (according to Eq. (3)) until finally the stability field of magnetite is reached (Fig. 9). As the coupled dissolution-reprecipitation reactions

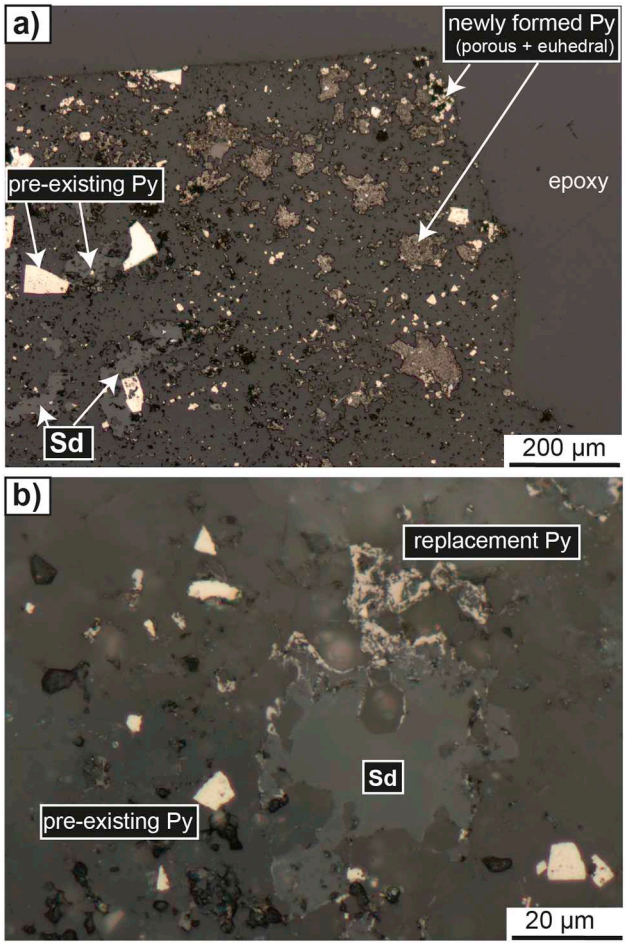

Fig. 4. Replacement texture of natural siderite in pyritic black shale; a) formation of porous pyrite and pervasive infiltration of H_2S containing fluid; b) direct observation of siderite replacement.

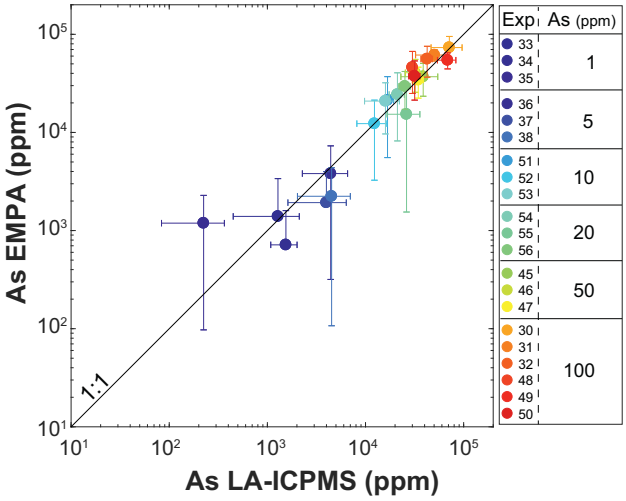

Fig. 5. Comparison of As concentrations of euhedral pyrite quantified by EMPA and LA-ICP-MS including 1:1 line, large spot size of LA-ICP-MS potentially underestimates As of euhedral pyrite as also pyrrhotite (having low As) is analyzed, error bars represent s.d. of multiple measurements with EMPA (n = 13–54) and LA-ICPMS (n = 3–11).

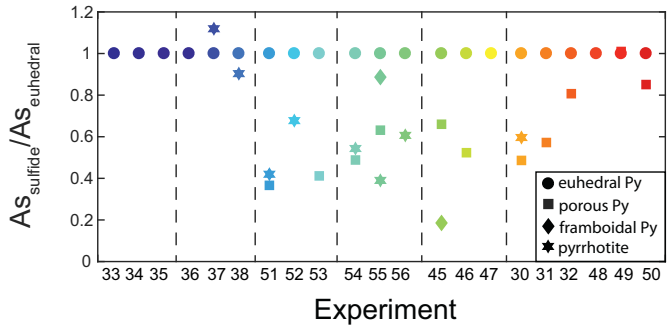

Fig. 6. Average arsenic concentrations of different coexisting sulfide types normalized to concentrations of euhedral pyrite showing a generally lower As concentration in porous and framboidal pyrite as well as for coexisting pyrrhotite.

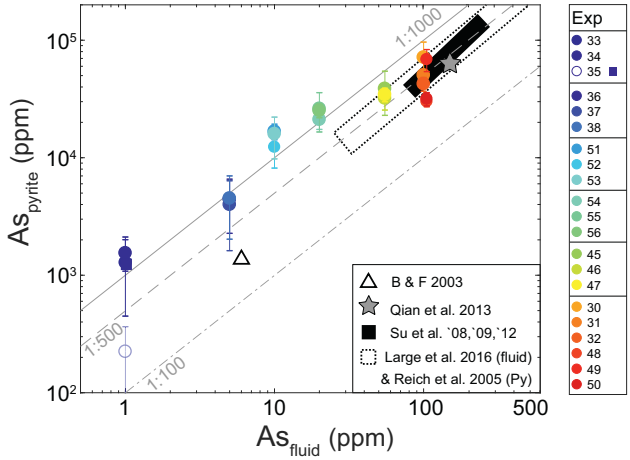

Fig. 7. Concentration of As of euhedral pyrite as a function of As concentration in the fluid, points: LA-ICP-MS data, square: EMPA data (only for exp. 35); including calculated As data for replacement experiments of Qian et al. (2013) and sorption experiments of Bostick and Fendorf (2003) as well as fluid inclusion and pyrite data for natural CTGD systems from China (Su et al., 2009; Su et al., 2008; Su et al., 2012) and Nevada (Large et al., 2016; Reich et al., 2005).

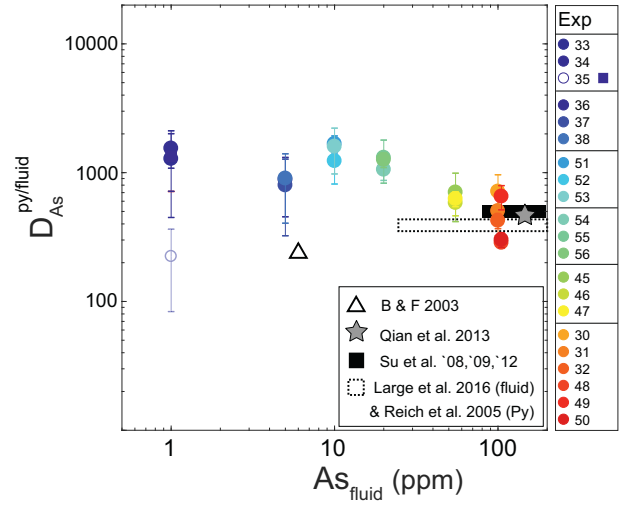

Fig. 8. Experimentally derived D values as a function of fluid concentration, in comparison D values calculated using published fluid and pyrite data from experimental studies and natural CTGDs as in Fig. 7.

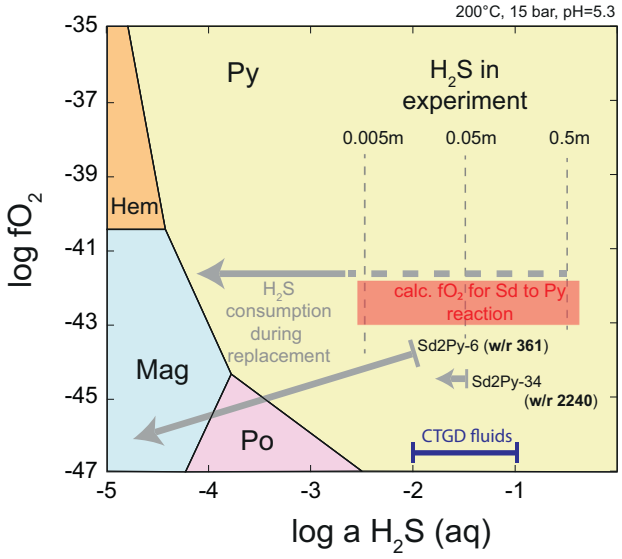

Fig. 9. Stability fields of Fe bearing mineral phases in the experimental system as a function of oxygen fugacity and H_2S activity; stability fields were calculated using the PHREEQC software package applying the implemented 'llnl' database, calculations were done at 200 °C, 15 bar and a pH of 5.3, calculated fO_2 for siderite replacement is −42.8; dotted lines: H_2S concentrations of experiments studying H_2S dependency; grey arrows showing possible H_2S evolution during replacement experiments, length representing H_2S consumption during experiments, which depends on fluid-to-rock ratio of the experiment.

penetrate from rim to core, early phases (i.e., pyrite) found in the rim regions form under high H_2S fugacity, whereas phases in core areas (i.e., magnetite) represent low H_2S conditions. Once the sulfides are formed under local equilibrium they are kinetically hindered to react further and will not re-equilibrate during experimental run times. Evolution of the H_2S activity can be either 'global' for the whole fluid present in the beaker, or only local for the interface fluid present at the boundaries of replacing phases. Given the large voids between replacement phases, stability of new phases is likely the result of a compositional evolution of the whole fluid, rather than controlled by local equilibria or diffusion from the bulk to the interfacial fluid. The equilibrium formation and, in particular, the stability of pyrrhotite implies very low oxygen fugacity values (a minimum $\log fO_2$ of −44) according to thermodynamic calculations (triple point at experimental conditions in Fig. 9). Thermodynamic stability fields of mineral phases were calculated as a function of fO_2 and aH_2S using the PHREEQC software package (Parkhurst and Appelo, 2013) for experimental conditions and starting compositions (Fig. 9). Calculated $\log fO_2$ for the reaction of siderite replacement is ~−43 for all compositions used in our experiments and is at odds with the formation of Po in our samples (Fig. 9).

The second explanation utilizes the observation that pyrite often forms from a precursor sulfide phase (Benning et al., 2000; Qian et al., 2010; Schoonen and Barnes, 1991a) via various pathways (i.e., polysulfide, Fe-loss, sulfidation). Metastable pyrrhotite was found to act as a precursor phase at high temperature (Qian et al., 2010) as it shows a high nucleation rate at a low oversaturation. In the case of siderite replacement, the localized release of Fe during dissolution of siderite (and additionally the subsequent precipitation of sulfides) will lead to conditions far from equilibrium, in which pyrrhotite might easily form as a metastable phase. With increasing reaction time, the system will equilibrate and pyrite will form as the stable sulfide phase. Nevertheless, transformation of the precursor phase pyrrhotite into pyrite is complex and remnants can form inclusions in newly growing pyrite as characterized by overgrowth and intergrowth textures (Fig. 2c).

As a result of the observations made from replacement experiments with varying H_2S concentrations, we adjusted our experimental setup for further investigation towards higher fluid-mineral ratios to avoid a compositional evolution during the experiment (Fig. 9).

4.1.2. pH dependent replacement features

In general, formation of sulfides via replacement of siderite is a very fast process and complete replacement is achieved within a few hours at low pH. We interpret the larger crystals and the predominance of euhedral over porous pyrite as being the results of recrystallization and crystal growth that increases with time and decreases with pH (Fig. 3). Under alkaline conditions replacement is slower and remnants of siderite persist in the core region of the former grains. Nevertheless, replacement is effective also at higher pH and the vast majority of the carbonate is replaced within 48 h. Compared to the experimental replacement of magnetite or pyrrhotite done at similar conditions (i.e., pH, temperature, fluid-mineral ratio, grain size and fluid composition) (Qian et al., 2010; Qian et al., 2011), siderite replacement is at least one order of magnitude faster at all pH conditions. Furthermore, magnetite and pyrrhotite replacement rarely reached completion within the experimental time, whereas almost all of our experiments using siderite show a complete replacement.

The observed pH and time dependencies of replacement suggest either generally slower reaction rates at alkaline pH or a change in the rate limiting process as a function of pH. The rate of a coupled dissolution-reprecipitation reaction is controlled by the slowest rate of all processes involved (i.e., dissolution, transport, precipitation). At low $pH_{25°C}$ we observe the formation of a blackish 'film' (likely composed of nm-sized Fe-sulfides) on the autoclave walls. The precipitation of this 'film' on autoclave walls is interpreted to represent a long-range solution transport of Fe, which is not instantaneously incorporated into replacement sulfides. Hence, it indicates a faster dissolution rate of Fe-carbonate compared to the precipitation rate of pyrite (Qian et al., 2010). Contrastingly, no precipitation on the autoclave walls at $pH_{25°C} > 5$ indicate an immediate incorporation of dissolved Fe into newly formed pyrite. In this case, dissolution becomes the rate limiting step and replacement shows short length scale pseudomorphism (Xia et al., 2009). Unlike in the case of U scavenging during replacement of magnetite by sulfides (Li et al., 2015), we do not observe a dependency of replacement features (e.g., zonation, rates) on trace element concentrations.

4.2. Similarities to natural Carlin type deposits

The main difference between the sediment experiments and pure siderite experiments is in the degree or progress of replacement. In the pure siderite system replacement was always complete at high H_2S concentrations, in the natural rock samples siderite is either still present in cores of the reacted sediment chips or in the process of being replaced (Fig. 4b). Additionally, newly formed pyrite is mainly found in the outer part of rock chips (Fig. 4a). These findings suggest that overall replacement rates are slower when sediment is used in the experiments. In this case, the transport of S from the bulk fluid towards the reaction interface (i.e., siderite domain within the black shale) is likely the rate limiting step as S needs to be transported via diffusion in pores or along grain boundaries. Nevertheless, once replacement of the carbonate starts it creates porosity due to the lower molar volume of pyrite compared to siderite which then enhances the transport capabilities. This effect will also apply for formation of ore stage pyrite in CTGD, where sedimentary layers rich in Fe-carbonates will be preferred sites for replacement.

Experimentally derived replacement textures share similarities to pyrite textures of natural Carlin type deposits. Apart from overgrowth on preexisting pyrite, natural CTGDs exhibit 'spongy', 'massive-porous' and disseminated pyrite of hydrothermal origin forming the main stage ore (Kesler et al., 2003; Large et al., 2009; Simon et al., 1999b; Su et al., 2008). In general these textures are interpreted to be the result of

replacement. As shown by our experiments, replacement of siderite in sedimentary host rocks can lead to highly porous pyrite but also to aggregations of μm-sized euhedral to anhedral pyrite due to recrystallization; these are very similar to common features of pyrite of CTGD (Saunders et al., 2014).

Although some features of CTGD were reproduced experimentally, prominent overgrowths of arsenian pyrite were almost never observed, neither in pure siderite experiments where 1–3 grains of seed-pyrite were added, nor in black-shale experiments that contained preexisting pyrite. A μm sized overgrowth of irregularly shaped arsenian pyrite was only formed in low pH (~4.4) experiments (Fig. 1b). These are the same experiments that showed a precipitation of sulfides on the beaker walls (see Section 4.1.2) and were interpreted to represent conditions under which dissolution of siderite is faster than precipitation of pyrite. Consequently, slightly acidic conditions are needed to produce an overgrowth on existing seed pyrite. In all other experiments at higher pH values, the precipitation of pyrite is more effective in suppressing Fe mobility and transport and, therefore, suppressing overgrowth textures. In both experimental setups Fe-carbonate is the only source of reactive iron, whereas in natural CTDG systems, other phases or fluids contribute to the overall amount of reactive iron, which might then be used to produce overgrowths on existing pre-ore pyrite. Additionally, replacement of pre-existing pyrite by ore stage pyrite via coupled dissolution-reprecipitation can lead to textures that look similar to overgrowth textures (Fleet and Mumin, 1997).

4.3. Arsenic substitution and arsenic solubility

Micro analytical measurements show that As concentrations in newly formed euhedral pyrite strongly correlate with decreasing S concentrations (Fig. 10a). We, therefore, conclude that As mainly replaces S in the pyrite structure and occurs therefore as As^{-1}, which is also the common species in Carlin type pyrite (Fleet and Mumin, 1997; Reich et al., 2005; Simon et al., 1999a; Simon et al., 1999b). Although, the correlation is distinctive it deviates from the 1:1 line. Consequently, around 25% of the As follows a different substitution mechanism. Although, correlation of As with Fe is less clear (Fig. 10b), pyrite having highest As of 4 mol% has reduced Fe (32 mol%) compared to stoichiometric pyrite with 33.3 mol% Fe. Therefore, other more oxidized species like As^{+2} or As^{+3} must substitute for Fe. This observation agrees with findings in natural and experimental arsenian pyrite (Deditius et al., 2014; Deditius et al., 2008; Le Pape et al., 2017; Qian et al., 2013).

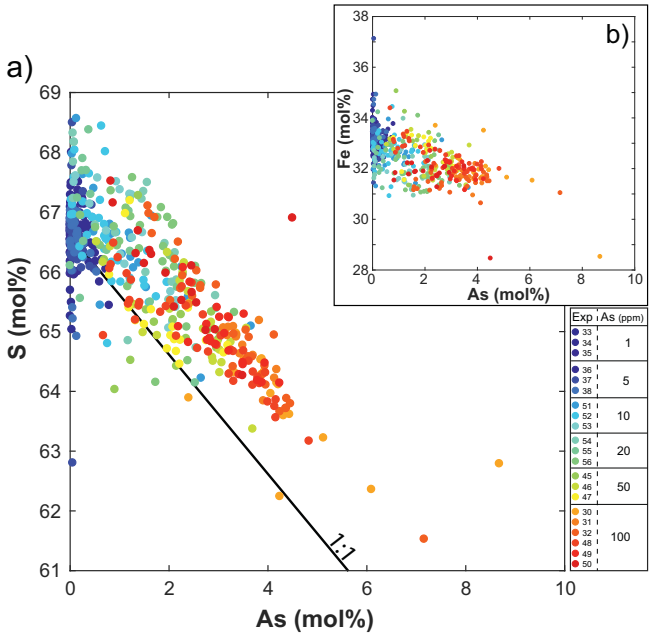

Fig. 10. Molar composition of euhedral pyrite formed during siderite replacement, a) strongly increasing As with decreasing S indicates the incorporation of As^{-1} as the major substitution process, b) the slightly negative trend with Fe indicates minor As substitution for Fe.

In comparison to other experimental studies, arsenian pyrite formed via replacement of siderite resembles results of arsenian pyrite formation via replacement of non-arsenian pyrite and pyrrhotite (Fleet and Mumin, 1997), rather than results of Qian et al. (2013), in which pyrite was formed via magnetite replacement. Maximum As concentration of our euhedral pyrite is similar to the experimental observations of Fleet and Mumin (1997) and does not exceed 7–8 wt%. This is in agreement with thermodynamic calculations that find a miscibility gap between pyrite and arsenopyrite in the system FeS_2-$FeAs_2$ showing a solubility limit of As in pyrite at around 7 wt% at 500 K (Reich and Becker, 2006). End member arsenopyrite was rarely identified to coexist with arsenian pyrite in experiments with the highest As concentrations (50–100 ppm). Nevertheless, a few EMPA analyses show As values higher than 8 wt%; this potentially indicates an intergrowth of pyrite and arsenopyrite at the nanoscale (Reich and Becker, 2006; Simon et al., 1999a, 1999b). When As substitutes for Fe as As^{+2} its concentrations can be as high as ~24 wt% due to a different substitution mechanism (Qian et al., 2013).

In nature, the occurrence of different As species in hydrothermal pyrite can be attributed to a different oxygen fugacity of the individual system. Under oxidizing conditions, typical for high-sulfidation systems, cationic As ($As^{+2,+3}$) is the dominant species in arsenian pyrite (Deditius et al., 2014; Deditius et al., 2008; Qian et al., 2013), whereas substitution of anionic As^{-1} is preferred in more reducing environments like that of Carlin type deposit. The similar behavior of As incorporation into pyrite during experimental siderite replacement and in pyrite from natural CTDGs confirm the general idea that ore stage arsenian pyrite of CTGSs is derived from replacement of Fe-carbonates present in the sedimentary wall rocks.

4.4. As partition coefficients in nature and experiments

Our experimental partition coefficients largely agree with observations and calculated D values of other natural and experimental fluid-pyrite systems that have similar conditions (i.e., T, major and trace element composition, pH, fluid to rock/mineral ratio, As speciation). In general, experimental and field studies reporting As trace element compositions of pyrite and coexisting/related fluid are rare and none of them report D values. Qian et al. (2013) published experimental data that can be used to calculate partition coefficients. As the authors did not publish fluid compositions but stated weights of all As containing solids they used, we estimated As concentration in their experimental runs from these data assuming reported complete dissolution of the As bearing phases. Concentration of As in their experimental fluids range from 24 to 220 ppm corresponding to maximum As of coexisting pyrite of 0.26 wt% up to 24 wt%, respectively. For the calculation of the D value we used reported maximum As concentrations. Arsenian pyrite in their experiments formed via a coupled dissolution-reprecipitation process of magnetite and highest As concentrations were always measured in the outermost rim, that was in contact with the hydrothermal fluids. Furthermore, this As-rich rim also shows features of recrystallization and was therefore in local equilibrium with the As-bearing fluid. Calculated D values range between 100 and 1600 for their experiments. Although their experimental conditions are different from ours, their calculated D values are very similar to our D values. Using data from the most similar experiment to ours (i.e., A11) from Qian et al. (2013) the calculated D value of 416 fits our results (Fig. 8). This is interesting as the substitution process of As into newly formed pyrite in the case of magnetite replacement (As for Fe) is different than in the case of siderite replacement (As for S).

In natural systems, partition coefficients can be inferred by using

compositions of fluid inclusions that represent the hydrothermal fluid that coexisted with pyrite. In CTGD, the lack of large fluid inclusions, the high detection limits and low concentrations of trace elements in individual fluid inclusions means that fluid trace element data is rare and only a few studies exist that published As values for fluids and pyrite. In a series of papers Su et al. (2008, 2009, 2012) reported trace element data for gold-bearing arsenian pyrite as well as data for co-existing fluid inclusions from Shuiyindong and Yata CTG deposits (Guizhou, China). Ore stage pyrite contains between 3.4 and 14 wt% As that substitutes for S in the pyrite structure. Related ore stage fluid inclusions were analyzed by LA-ICP-MS and range from 80 to 250 ppm. Assuming that As in pyrite correlates positively with As in fluid, calculated partition coefficients are between 437 and 560. Similar values can be calculated for the Golden Quarry CTGD from Nevada using recently published fluid inclusion data by Large et al. (2016) combined with general data for pyrite from the Carlin trend deposits (Deditius et al., 2014; Arehart et al., 1993). Measured fluid inclusion data for As range from 24 to 540 ppm and span a slightly larger range than CTDGs from China. It should be noted, however that As concentrations in many of the analyzed fluid inclusions are below the detection limit and, therefore, true As concentrations of the hydrothermal fluid are likely lower than the averaged values. Concentration of As in coeval pyrite is stated as being ~2–6 wt% (Large et al., 2016), which agrees with more precise data for ore stage pyrite (3.7–5.4 wt% As) from the same deposit (Arehart et al., 1993). In general, ore stage arsenian pyrite from CTGDs from Nevada has maximum As concentration of 19 wt%, that can decrease to ~1 wt% in some deposits (Reich et al., 2005). Given these large variabilities in fluid and pyrite composition, D values for highest and lowest reported concentrations of ore stage arsenian pyrite are calculated to be in the range of 350 to 420.

The inferred partition coefficients of our experimental study as well as of natural CTGD systems are in strong disagreement with the only other publication stating D values. Deditius et al. (2014) suggest very low D values for As in the order of 0.02 to 0.2 based on fluid inclusion and pyrite data from the Rosia-Poieni porphyry/epithermal Cu-Au deposit (Kouzmanov et al., 2010). Although element partitioning should be stable over a large range of conditions and composition, several differences between CTGD and epithermal deposits might lead to the discrepancy of 4 orders of magnitude in calculated D values: 1) the higher temperature of the epithermal systems (250–350 °C) compared to CTGD systems (< 220 °C) might lead to changes in the partitioning behavior as pyrite has retrograde solid solubility of As with temperature (Deditius et al., 2014). This behavior can be explained by kinetic factors which in turn might influence partitioning as they affect recrystallization of sulfides before reaching equilibrium. In particular, far from equilibrium conditions at low temperatures might lead to varying D values. Temperature dependent kinetics also influence fundamental processes involved during incorporation of As into pyrite like the rates of adsorption and growth. 2) An additional change in partition behavior might be caused by strongly differing pH values of epithermal (extremely acidic; Kouzmanov et al., 2010) and CTG (slightly acidic to neutral; Saunders et al., 2014) deposits. 3) Rosia-Poieni epithermal veins contain, apart from pyrite, large amounts of enargite (Cu_3AsS_4) which acts as a potential sink for As and conflicts with equilibrium partitioning between fluid and pyrite. 4) A potential different speciation of As in the fluid can cause different partitioning. Qian et al. (2013) showed in their experiments that As dissolved from solids containing anionic As (i.e., loellingite, arsenopyrite) is incorporated much less into pyrite compared to As from sources containing cationic As (e.g., realgar, As_2O_3). Although, this argument seems counterintuitive as conditions of epithermal deposits are more oxidizing and should favor cationic $As^{+3,+5}$, findings of Qian et al. (2013) are independent of oxygen fugacity and seem only to rely on the speciation of As in source phases. The chemical state of arsenic in enargite, which is the major As bearing phase in the epithermal sample, is very similar to arsenides and, therefore, similar to loellingite and arsenopyrite (Fantauzzi et al., 2006). Consequently, As dissolved from enargite is not incorporated into pyrite and calculated D values from the Rosia-Poieni epithermal system will be unusually low.

4.5. Implication of high partitioning for pyrite systems

Although the preferential incorporation of As into pyrite has been suggested for different types of ore deposits, this study quantifies partition coefficients for sulfidation systems at moderate temperatures like CTGD, sediment hosted massive sulfide and epithermal deposits. The derived D values can not only be used to estimate the composition of ore fluids from the As concentration of pyrite, but can help to explain the large variation of As in pyrite observed in these deposits. In general, μm scale variations of As (and other trace elements) in pyrite producing a growth zonation are explained by changes in fluid composition due to various processes like mixing, boiling or exsolution (Deditius et al., 2009; Feng et al., 2017; Peterson and Mavrogenes, 2014; Tardani et al., 2017; Yan et al., 2018). Taking the high D values into account, parts of the zonation showing decreasing As concentrations can be attributed to compositional evolution of the fluid caused by the effective incorporation of As into the pyrite overgrowth. Repeated replenishment with an enriched fluid will lead to oscillating zonations which are frequently observed in pyrite. On the scale of individual CTGDs, the overall variation of As found in different types of ore stage pyrite (i.e., porous, overgrowth, disseminated) ranging from ~1 up to 19 wt% might also be caused by the evolution of As in the hydrothermal fluid as a result of equilibrium fractionation of a single fluid event.

4.6. Control of incorporation of As into hydrothermal pyrite

Partitioning experiments were designed to mimic conditions and compositions of natural CTGDs and the calculated partition coefficients are purely empirical. They allow only limited insights into the exact processes that controlled the partitioning of As into pyrite during growth. In a simplistic way, one can think of two individual factors and related processes that govern the incorporation at low to hydrothermal temperatures: 1) the solid solubility of As in pyrite (maximum around 7–8 wt% at conditions of interest) which is controlled by the crystallographic structure; 2) surface controlled sorption of As onto the growing pyrite. The first factor is a function of intrinsic variables and ultimately controlled by Gibbs free energy minimization of the solid solution and is, therefore, the major control for partitioning at high temperatures (e.g., melt systems, sub solidus diffusional exchange) as described for example by the lattice strain model (Blundy and Wood, 1994). In low temperature, fluid mediated environments the adsorption capability onto mineral surfaces becomes more important for partitioning as it controls the availability of the substituent during crystal growth. Given that the intrinsic factors controlled by the crystal lattice of pyrite allow for perfect solid solution (< 7 wt% As), sorption of As onto the reactive pyrite surface controls partitioning in our experiments as well as in natural systems. Often the formation of arsenian pyrite (and coeval Au enrichment) in low T settings is referred to as a surface and kinetically controlled process (Deditius et al., 2014; Fleet and Mumin, 1997; Palenik et al., 2004; Qian et al., 2013) that enables the reduction of the dissolved species As^{3+} (either as $As^{3+}(OH)_3$ or as thio-complexes in presence of H_2S and low pH (Keller et al., 2014)) to As^{-1} in pyrite. Sorption experiments at ambient temperatures show a high adsorption capacity of As onto sulfide surfaces that can be described by common sorption isotherms (i.e., Freundlich and/or Langmuir isotherms). Isotherms, in general, relate the amount of an adsorbed element onto a mineral to concentration of sorbent in fluids (Bostick and Fendorf, 2003; Farquhar et al., 2002; Han et al., 2013; Wolthers et al., 2005) and simple Nernst partition coefficients can be seen in this context to be one form of a linear isotherm expression. For As, the observed maximum adsorption on pyrite at ambient temperatures is around 2310–270 μmol/g relating to a surface coverage of 5.6 μmol/m^2

(Bostick and Fendorf, 2003; Han et al., 2013) which correspond to a concentration of ~2 wt% As in pyrite assuming that all adsorbed As is incorporated during growth. Interestingly, the empirically gained adsorption maxima and the thermodynamically calculated solubility limit (~4 wt% As at ambient conditions (Reich and Becker, 2006)) are very similar and differ only by a factor of 2. The shape and maxima of the isotherms, and therefore the relationship of As adsorption to As concentration in fluid, strongly depends on pH but also on H_2S and likely temperature (Bostick and Fendorf, 2003). In the absence of high temperature experiments, sorption behavior of As at hydrothermal conditions is largely unknown. Although, it is therefore impossible to extract exact partitioning values from low temperature sorption experiments, the linear correlation in As adsorption observed by Bostick and Fendorf (2003) for H_2S-rich systems can be used to calculate D values of around 250 which agrees with D values of our experiments.

The similarities between adsorption onto, and partitioning into, pyrite indicate a potential coupling of the two processes working during trace element distribution in hydrothermal systems like Carlin. Consequently, the high variance in composition of pyrite from these systems is a direct result from changes in the local environment (compositionally and kinetically) that in turn changes the adsorption behavior onto a growing surface.

5. Conclusion

Fluid mediated replacement of siderite by pyrite is a fast and effective process to transform Fe-bearing carbonates into sulfides that works via a coupled dissolution-reprecipitation reaction. New pyrite forms either as cluster of dense euhedral grains under acidic pH conditions or as a porous mass under alkaline pH that recrystallizes with time to form euhedral to anhedral pyrite grains or clusters.

Experimental partitioning of As between hydrothermal fluid and newly formed euhedral pyrite have partition coefficients in the range of 286 to 1676 that are similar to D values calculated from literature data for natural and experimental pyrite systems. Arsenic in pyrite formed via siderite replacement is mainly substituting for S and, therefore, bound as anionic As^{-1} in the pyrite structure.

Findings of this experimental study are similar to observations made in natural Carlin-type gold deposits and confirm the general idea that arsenian pyrite of these deposits forms via replacement of Fe-carbonates like siderite. The newly constrained partition coefficients for As are able to explain the large heterogeneity in CTGD pyrite compositions which is caused by a compositional evolution of the fluid due to the strong fractionation of As into the forming pyrite and, therefore, depletion in the fluid.

Supplementary data to this article can be found online at https://doi.org/10.1016/j.chemgeo.2018.09.027.

Acknowledgements

All authors acknowledge the financial support of the Helmholtz Recruitment Initiative to S. Gleeson. We thank Jan Müller and Joseph M. Magnall for supplying samples and Johannes Glodny for the experimental equipment. Further, we thank Judith Schicks for assistance with the Raman spectroscopy and Oona Appelt and Franziska Wilke for their assistance carrying out the EMPA data. Helpful comments from M. Reich and an anonymous reviewer improved this manuscript.

References

Arehart, G.B., Chryssoulis, S.L., Kesler, S.E., 1993. Gold and arsenic in iron sulfides from sediment-hosted disseminated gold deposits - implications for depositional processes. Econ. Geol. Bull. Soc. Econ. Geol. 88 (1), 171–185.

Benning, L.G., Wilkin, R.T., Barnes, H.L., 2000. Reaction pathways in the Fe-S system below 100 degrees C. Chem. Geol. 167 (1–2), 25–51.

Blundy, J., Wood, B., 1994. Prediction of crystal-melt partition-coefficients from elastic-moduli. Nature 372 (6505), 452–454. https://doi.org/10.1038/372452a0.

Bostick, B.C., Fendorf, S., 2003. Arsenite sorption on troilite (FeS) and pyrite (FeS2). Geochim. Cosmochim. Acta 67 (5), 909–921. https://doi.org/10.1016/s0016-7037(02)01170-5.

Cail, T.L., Cline, J.S., 2001. Alteration associated with gold deposition at the Getchell Carlin-type gold deposit, north-central Nevada. Econ. Geol. Bull. Soc. Econ. Geol. 96 (6), 1343–1359. https://doi.org/10.2113/96.6.1343.

Cline, J.S., Hofstra, A.H., Muntean, J.L., Tosdal, R.M., Hickey, K.A., 2005. Carlin-Type Gold Deposits in Nevada: Critical Geologic Characteristics and Viable Models. Vol. 451 Economic Geology and the Bulletin of the Society of Economic Geologists (100th Anni).

Deditius, A.P., et al., 2008. A proposed new type of arsenian pyrite: composition, nanostructure and geological significance. Geochim. Cosmochim. Acta 72 (12), 2919–2933. https://doi.org/10.1016/j.gca.2008.03.014.

Deditius, A.P., et al., 2009. Decoupled geochemical behavior of As and Cu in hydrothermal systems. Geology 37 (8), 707–710. https://doi.org/10.1130/g25781a.1.

Deditius, A.P., et al., 2014. The coupled geochemistry of Au and As in pyrite from hydrothermal ore deposits. Geochim. Cosmochim. Acta 140, 644–670. https://doi.org/10.1016/j.gca.2014.05.045.

Emsbo, P., Hofstra, A.H., Lauha, E.A., Griffin, G.L., Hutchinson, R.W., 2003. Origin of high-grade gold ore, source of ore fluid components, and genesis of the Meikle and neighboring Carlin-type deposits, northern Carlin trend, Nevada. Econ. Geol. Bull. Soc. Econ. Geol. 98 (6), 1069–1105. https://doi.org/10.2113/98.6.1069.

Fantauzzi, M., Atzei, D., Elsener, B., Lattanzi, P., Rossi, A., 2006. XPS and XAES analysis of copper, arsenic and sulfur chemical state in enargites. Surf. Interface Anal. 38 (5), 922–930. https://doi.org/10.1002/sia.2348.

Farquhar, M.L., Charnock, J.M., Livens, F.R., Vaughan, D.J., 2002. Mechanisms of arsenic uptake from aqueous solution by interaction with goethite, lepidocrocite, mackinawite, and pyrite: an X-ray absorption spectroscopy study. Environ. Sci. Technol. 36 (8), 1757–1762. https://doi.org/10.1021/es010216g.

Feng, K., et al., 2017. Involvement of anomalously As-Au-rich fluids in the mineralization of the Heilan'gou gold deposit, Jiaodong, China: evidence from trace element mapping and in-situ sulfur isotope composition. J. Asian Earth Sci. https://doi.org/10.1016/j.jseaes.2017.12.023.

Fleet, M.E., Mumin, A.H., 1997. Gold-bearing arsenian pyrite and marcasite and arsenopyrite from Carlin Trend gold deposits and laboratory synthesis. Am. Mineral. 82 (1–2), 182–193.

Han, D.S., Song, J.K., Batchelor, B., Abdel-Wahab, A., 2013. Removal of arsenite (As(III)) and arsenate(As(V)) by synthetic pyrite (FeS_2): synthesis, effect of contact time, and sorption/desorption envelopes. J. Colloid Interface Sci. 392, 311–318. https://doi.org/10.1016/j.jcis.2012.09.084.

Hofstra, A.H., Cline, J.S., 2000. Characteristics and models for Carlin-type gold deposits. In: Hagemann, S.G., Brown, E.B. (Eds.), Reviews in Economic Geology, pp. 163–220.

Hofstra, A.H., et al., 1991. Genesis of sediment-hosted disseminated-gold deposits by fluid mixing and sulfidization - chemical-reaction-path modeling of ore-depositional processes documented in the Jerritt Canyon District, Nevada. Geology 19 (1), 36–40.

Keller, N.S., Stefánsson, A., Sigfússon, B., 2014. Arsenic speciation in natural sulfidic geothermal waters. Geochim. Cosmochim. Acta 142, 15–26. https://doi.org/10.1016/j.gca.2014.08.007.

Kesler, S.E., et al., 2003. Evaluation of the role of sulfidation in deposition of gold, Screamer section of the Betze-Post Carlin-type deposit, Nevada. Econ. Geol. Bull. Soc. Econ. Geol. 98 (6), 1137–1157. https://doi.org/10.2113/98.6.1137.

Kouzmanov, K., Pettke, T., Heinrich, C.A., 2010. Direct analysis of ore-precipitating fluids: combined IR microscopy and LA-ICP-MS study of fluid inclusions in opaque ore minerals. Econ. Geol. 105 (2), 351–373.

Large, R.R., et al., 2009. Gold and trace element zonation in pyrite using a laser imaging technique: implications for the timing of gold in orogenic and Carlin-style sediment-hosted deposits. Econ. Geol. 104 (5), 635–668.

Large, R.R., Bull, S.W., Maslennikov, V.V., 2011. A carbonaceous sedimentary source-rock model for Carlin-type and orogenic gold deposits. Econ. Geol. 106 (3), 331–358. https://doi.org/10.2113/econgeo.106.3.331.

Large, S.J.E., et al., 2016. Trace elements in fluid inclusions of sediment-hosted gold deposits indicate a magmatic-hydrothermal origin of the Carlin ore trend. Geology 44 (12), 1015–1018. https://doi.org/10.1130/g38351.1.

Le Pape, P., et al., 2017. Arsenic incorporation in pyrite at ambient temperature at both tetrahedral S(-I) and octahedral Fe(II) sites: evidence from EXAFS-DFT analysis. Environ. Sci. Technol. 51 (1), 150–158. https://doi.org/10.1021/acs.est.6b03502.

Li, K., et al., 2015. Uranium scavenging during mineral replacement reactions. Am. Mineral. 100 (8–9), 1728–1735. https://doi.org/10.2138/am-2015-5125.

Magnall, J.M., Gleeson, S.A., Blamey, N.J.F., Paradis, S., Luo, Y., 2016. The thermal and chemical evolution of hydrothermal vent fluids in shale hosted massive sulphide (SHMS) systems from the MacMillan Pass district (Yukon, Canada). Geochim. Cosmochim. Acta 193, 251–273. https://doi.org/10.1016/j.gca.2016.07.020.

Muntean, J.L., Cline, J.S., Simon, A.C., Longo, A.A., 2011. Magmatic–hydrothermal origin of Nevada's Carlin-type gold deposits. Nat. Geosci. 4 (2), 122–127. https://doi.org/10.1038/ngeo1064.

Palenik, C.S., et al., 2004. "Invisible" gold revealed: direct imaging of gold nanoparticles in a Carlin-type deposit. Am. Mineral. 89 (10), 1359–1366.

Parkhurst, D.L., Appelo, C., 2013. Description of Input and Examples for PHREEQC Version 3: A Computer Program for Speciation, Batch-Reaction, One-Dimensional Transport, and Inverse Geochemical Calculations. US Geological Survey, pp. 2328–7055.

Paton, C., Hellstrom, J., Paul, B., Woodhead, J., Hergt, J., 2011. Iolite: freeware for the visualisation and processing of mass spectrometric data. J. Anal. At. Spectrom. 26 (12), 2508. https://doi.org/10.1039/c1ja10172b.

Peterson, E.C., Mavrogenes, J.A., 2014. Linking high-grade gold mineralization to earthquake-induced fault-valve processes in the Porgera gold deposit, Papua New

Guinea. Geology 42 (5), 383–386. https://doi.org/10.1130/g35286.1.
Putnis, A., 2002. Mineral replacement reactions: from macroscopic observations to microscopic mechanisms. Mineral. Mag. 66 (5), 689–708.
Qian, G., Brugger, J., Skinner, W.M., Chen, G., Pring, A., 2010. An experimental study of the mechanism of the replacement of magnetite by pyrite up to 300 °C. Geochim. Cosmochim. Acta 74 (19), 5610–5630. https://doi.org/10.1016/j.gca.2010.06.035.
Qian, G., et al., 2011. Replacement of pyrrhotite by pyrite and marcasite under hydrothermal conditions up to 220 °C: an experimental study of reaction textures and mechanisms. Am. Mineral. 96 (11 − 12), 1878–1893. https://doi.org/10.2138/am.2011.3691.
Qian, G., Brugger, J., Testemale, D., Skinner, W., Pring, A., 2013. Formation of As(II)-pyrite during experimental replacement of magnetite under hydrothermal conditions. Geochim. Cosmochim. Acta 100, 1–10. https://doi.org/10.1016/j.gca.2012.09.034.
Reich, M., Becker, U., 2006. First-principles calculations of the thermodynamic mixing properties of arsenic incorporation into pyrite and marcasite. Chem. Geol. 225 (3–4), 278–290. https://doi.org/10.1016/j.chemgeo.2005.08.021.
Reich, M., et al., 2005. Solubility of gold in arsenian pyrite. Geochim. Cosmochim. Acta 69 (11), 2781–2796. https://doi.org/10.1016/j.gca.2005.01.011.
Saunders, J.A., Hofstra, A.H., Goldfarb, R.J., Reed, M.H., 2014. Geochemistry of hydrothermal gold deposits 13.15. In: Holland, H.D., Turekian, K.K. (Eds.), Treatise on Geochemistry, Second Edition. Elsevier, Oxford, pp. 383–424.
Schoonen, M.A.A., Barnes, H.L., 1991a. Mechanisms of pyrite and marcasite formation from solution 3. Hydrothermal processes. Geochim. Cosmochim. Acta 55 (12), 3491–3504. https://doi.org/10.1016/0016-7037(91)90050-F.
Schoonen, M.A.A., Barnes, H.L., 1991b. Reactions forming pyrite and marcasite from solution 1. Nucleation of FeS_2 below 100 °C. Geochim. Cosmochim. Acta 55 (6), 1495–1504. https://doi.org/10.1016/0016-7037(91)90122-L.
Schoonen, M.A.A., Barnes, H.L., 1991c. Reactions forming pyrite and marcasite from solution 2. Via Fes precursors below 100 °C. Geochim. Cosmochim. Acta 55 (6), 1505–1514. https://doi.org/10.1016/0016-7037(91)90123-M.
Simon, G., Huang, H., Penner-Hahn, J.E., Kesler, S.E., Kao, L.S., 1999a. Oxidation state of gold and arsenic in gold-bearing arsenian pyrite. Am. Mineral. 84 (7–8), 1071–1079.
Simon, G., Kesler, S.E., Chryssoulis, S., 1999b. Geochemistry and textures of gold-bearing arsenian pyrite, Twin Creeks, Nevada: Implications for deposition of gold in Carlin-type deposits. Econ. Geol. Bull. Soc. Econ. Geol. 94 (3), 405–421.
Stenger, D.P., Kesler, S.E., Peltonen, D.R., Tapper, C.J., 1998. Deposition of gold in Carlin-type deposits: the role of sulfidation and decarbonation at Twin Creeks, Nevada. Econ. Geol. Bull. Soc. Econ. Geol. 93 (2), 201–215. https://doi.org/10.2113/gsecongeo.93.2.201.
Su, W.C., Xia, B., Zhang, H.T., Zhang, X.C., Hu, R.Z., 2008. Visible gold in arsenian pyrite at the Shuiyindong Carlin-type gold deposit, Guizhou, China: implications for the environment and processes of ore formation. Ore Geol. Rev. 33 (3–4), 667–679. https://doi.org/10.1016/j.oregeorev.2007.10.002.
Su, W.C., et al., 2009. Sediment-hosted gold deposits in Guizhou, China: products of wall-rock sulfidation by deep crustal fluids. Econ. Geol. 104 (1), 73–93.
Su, W.C., et al., 2012. Mineralogy and geochemistry of gold-bearing arsenian pyrite from the Shuiyindong Carlin-type gold deposit, Guizhou, China: implications for gold depositional processes. Mineral. Deposita 47 (6), 653–662. https://doi.org/10.1007/s00126-011-0328-9.
Sung, Y.H., et al., 2009. Invisible gold in arsenian pyrite and arsenopyrite from a multistage Archaean gold deposit: sunrise Dam, Eastern Goldfields Province, Western Australia. Mineral. Deposita 44 (7), 765–791. https://doi.org/10.1007/s00126-009-0244-4.
Tardani, D., et al., 2017. Copper-arsenic decoupling in an active geothermal system: a link between pyrite and fluid composition. Geochim. Cosmochim. Acta 204, 179–204. https://doi.org/10.1016/j.gca.2017.01.044.
Thomas, H.V., et al., 2011. Pyrite and pyrrhotite textures and composition in sediments, laminated quartz veins, and reefs at Bendigo Gold Mine, Australia: insights for ore genesis. Econ. Geol. 106 (1), 1–31. https://doi.org/10.2113/econgeo.106.1.1.
Wolthers, M., Charlet, L., van Der Weijden, C.H., van der Linde, P.R., Rickard, D., 2005. Arsenic mobility in the ambient sulfidic environment: sorption of arsenic(V) and arsenic(III) onto disordered mackinawite. Geochim. Cosmochim. Acta 69 (14), 3483–3492. https://doi.org/10.1016/j.gca.2005.03.003.
Woodhead, J.D., Hellstrom, J., Hergt, J.M., Greig, A., Maas, R., 2007. Isotopic and elemental imaging of geological materials by laser ablation inductively coupled plasma-mass spectrometry. Geostand. Geoanal. Res. 31 (4), 331–343.
Xia, F., et al., 2009. Mechanism and kinetics of pseudomorphic mineral replacement reactions: a case study of the replacement of pentlandite by violarite. Geochim. Cosmochim. Acta 73 (7), 1945–1969. https://doi.org/10.1016/j.gca.2009.01.007.
Yan, J., et al., 2018. NanoSIMS element mapping and sulfur isotope analysis of Au-bearing pyrite from Lannigou Carlin-type Au deposit in SW China: new insights into the origin and evolution of Au-bearing fluids. Ore Geol. Rev. 92, 29–41. https://doi.org/10.1016/j.oregeorev.2017.10.015.
Ye, Z., Kesler, S.E., Essene, E.J., Zohar, P.B., Borhauer, J.L., 2002. Relation of Carlin-type gold mineralization to lithology, structure and alteration: screamer zone, Betze-Post deposit, Nevada. Mineral. Deposita 38 (1), 22–38. https://doi.org/10.1007/s00126-002-0265-8.